



# An Uncertainty-Quantification Machine Learning Framework for Data-Driven Three-Dimensional Mineral Prospectivity Mapping

Zhiqiang Zhang,<sup>1,2,3</sup> Gongwen Wang<sup>4,8</sup>, Emmanuel John M. Carranza,<sup>5</sup> Jingguo Du,<sup>6</sup> Yingjie Li,<sup>1,2,3</sup> Xinxing Liu,<sup>1,2,3</sup> and Yongjun Su<sup>7</sup>

Received 12 January 2024; accepted 13 April 2024

The uncertainty inherent in three-dimensional (3D) mineral prospectivity mapping (MPM) encompasses (a) mineral system conceptual model uncertainty stemming from geological conceptual frameworks, (b) aleatoric uncertainty, attributable to the variability and noise due to multi-source geoscience datasets collection and processing, as well as 3D geological modeling process, and (c) epistemic uncertainty due to predictive algorithm modeling. Quantifying the uncertainty of 3D MPM is a prerequisite for accepting predictive models in exploration. Previous MPM studies were centered on addressing the mineral system conceptual model uncertainty. To the best of our knowledge, few studies quantified the aleatoric and epistemic uncertainties of 3D MPM. This study proposes a novel uncertainty-quantification machine learning framework to qualify aleatoric and epistemic uncertainties in 3D MPM by the uncertainty-quantification random forest. Another innovation of this framework is utility of the accuracy–rejection curve to provide a quantitative uncertainty threshold for exploration target delineation. The Bayesian hyperparameter optimization tunes the hyperparameters of the uncertainty-quantification random forest automatically. The case study of 3D MPM for exploration target delineation in the Wulong gold district of China demonstrated the practicality of our framework. The aleatoric uncertainty of the 3D MPM indicates that the 3D Early Cretaceous dyke model is the main source of this uncertainty. The 3D exploration targets delineated by the uncertainty-quantification machine learning framework can benefit subsurface gold exploration in the study area.

**KEY WORDS:** Aleatoric uncertainty, Epistemic uncertainty, Uncertainty-quantification random forest, Accuracy–rejection curve, Three-dimensional mineral prospectivity mapping, Wulong gold district.

<sup>1</sup>Hebei Province Collaborative Innovation Center for Strategic Critical Mineral Research, Hebei GEO University, Shijiazhuang 050031, People's Republic of China.

<sup>2</sup>Hebei Key Laboratory of Strategic Critical Mineral Resources, Hebei GEO University, Shijiazhuang 050031, People's Republic of China.

<sup>3</sup>School of Earth Sciences, Hebei GEO University, Shijiazhuang 050031, People's Republic of China.

<sup>4</sup>MNR Key Laboratory for Exploration Theory and Technology of Critical Mineral Resources, China University of Geosciences, Beijing 100083, People's Republic of China.

<sup>5</sup>Geological of Geology, Faculty of Natural and Agricultural Sciences, University of the Free State, Bloemfontein, South Africa.

<sup>6</sup>School of Earth Science and Resources, Chang'an University, Xi'an 710054, People's Republic of China.

<sup>7</sup>Tianjin Center, China Geological Survey, Tianjin 300170, People's Republic of China.

<sup>8</sup>To whom correspondence should be addressed; e-mail: gwwang@cugb.edu.cn

## INTRODUCTION

Mineral prospectivity mapping (MPM) is a multi-step spatial quantitative process to identify systematically exploration targets or areas with high potential for exploration success (Agterberg, 1989). The working principle to delineate exploration targets is to integrate evidence layers in a geographic information system (GIS) (Agterberg, 1989; Carranza, 2008; Zuo et al., 2023). The evidence layers can be extracted from multi-source geoscience datasets based on exploration criteria, which in turn can be determined from understanding of relevant mineral systems (McCuaig et al., 2010; Burkin et al., 2019; Lindsay et al., 2022). Methods of MPM can be subdivided into data-driven and knowledge-driven methods (Agterberg, 1989; Carranza & Hale., 2001). Knowledge-driven methods (e.g., fuzzy logic and index overlays) are useful in “greenfields” with limited prior information about their mineral potential (Carranza & Hale., 2001; Harris et al., 2015). Data-driven methods (e.g., weights-of-evidence, Random Forest (RF), convolutional neural network) are suited for “brownfields” with extensive exploration history (Agterberg, 1989; Carranza & Laborte., 2015; Li et al., 2023). Both knowledge-driven and data-driven methods involve multiple steps, and uncertainties arise in each step, potentially impacting the final MPM results (cf. Kreuzer et al., 2008; Lisitsin et al., 2014; Burkin et al., 2019; Wang et al., 2020; Zuo et al., 2021; Zhang et al., 2022). Consequently, considering uncertainties during the prediction process is crucial in addition to predictive probability (cf. Porwal et al., 2006; Kreuzer et al., 2008; Burkin et al., 2019; Zuo et al., 2021; Lisitsin et al., 2022).

Over the long history of mining worldwide, most outcropping deposits have been discovered, mined and are nearly depleted (Ghorbani et al., 2023). Therefore, in the past decade, surface two-dimensional (2D) MPM has extended progressively to subsurface three-dimensional (3D) MPM (Payne et al., 2015; Wang et al., 2015; Li et al., 2016). Data-driven methods were commonly applied for 3D MPM because most of this work was undertaken in data-rich “brownfields” with known mining deposits (Yuan et al., 2014; Wang et al., 2015; Li et al., 2016). In 3D MPM research, several studies have focused on estimating the predictive probability of mineral deposit occurrence (Yuang et al., 2014; Payne et al., 2015; Zhang et al., 2021b; Li et al., 2023), as well as

estimating metal tenor and tonnage (Nielsen et al., 2019; Jordão et al., 2023; Mao et al., 2023a, b). To the best of our knowledge, limited investigations have quantified uncertainty in 3D MPM (Zhang et al., 2022). The uncertainty of data-driven 3D MPM can be subdivided as follows.

- (1) Mineral system conceptual model uncertainty: A mineral system refers to a geological conceptual framework, which consists of source, pathway, transport, and trap mechanisms that work together to form mineral deposits (Wyborn et al., 1994). Exploration criteria are determined based on a mineral system conceptual model (McCuaig et al., 2010; Burkin et al., 2019; Lindsay et al., 2022). However, a conceptual model of mineral system for the same type of deposits may be disputed due to a limited understanding of the critical ore-forming processes (Zuo et al., 2015; Burkin et al., 2019; Lindsay et al., 2022). The uncertainty associated with a mineral system conceptual model can lead to divergent exploration criteria within the same study area, subsequently impacting the results of MPM (Zuo et al., 2015; Burkin et al., 2019; Lindsay et al., 2022).
- (2) Aleatoric (or stochastic) uncertainty: The noise due to multi-source geoscience datasets collection and processing is a critical source of aleatoric uncertainty (Zuo et al., 2021; Yang et al., 2023). Besides, multi-source geoscience datasets are not directly suitable for input into data-driven 3D MPM (Deng et al., 2022; Mao et al., 2023a, b). To obtain the input evidence layers, a two-step process is typically followed. Firstly, a 3D geological model is constructed through the integration of multi-source geoscience datasets (Wang et al., 2015; Deng et al., 2022; Mao et al., 2023a, b). Secondly, evidence layers are extracted from the 3D geological model based on exploration criteria (Deng et al., 2022; Mao et al., 2023a, b). The extracted evidence layers can be used as input data for data-driven 3D MPM. Therefore, the aleatoric uncertainty in data-driven 3D MPM also arises from the inherent noise in evidence layers, which are related to a 3D geological model (Porwal et al., 2006; Kendall & Gal, 2017; Huang et al., 2022; Zhang et al., 2022).
- (3) Epistemic (systemic) uncertainty: This kind of uncertainty emerges from the process of evi-

dence layer integration, and it is related to whether the data-driven model parameters and hyperparameters can capture effectively the underlying ore-forming patterns present in the evidence layers (Porwal et al., 2006; Kendall & Gal, 2017; Wang et al., 2020). Examples of model parameters include the coefficients of features in logistic regression (Xiong & Zuo, 2018) and the bias of units in neural networks (Smith, 2018). Examples of model hyperparameters include the penalty type of logistic regression (Xiong & Zuo, 2018) and the batch size of neural networks (Smith, 2018).

A mineral system conceptual model influences the selection of evidence layers. Aleatoric uncertainty relates to the data quality within evidence layers, which are defined by the mineral system conceptual model, while epistemic uncertainty is related to the algorithm that integrates these evidence layers. Consequently, these three types of uncertainty propagate progressively through the MPM process, impacting the final results and the targeting process (Zuo et al., 2021). It is challenging to quantify and address mineral system conceptual model uncertainty in data-driven 3D MPM by mathematical modeling because it is a geological conceptual model. Zuo et al. (2015) and Lindsay et al. (2022) suggested to combine diverse MPM results derived from different mineral system conceptual models to address mineral system conceptual model uncertainty. Regarding aleatoric uncertainty in MPM, previous studies performed Monte Carlo simulation of hundreds of evidence layers for MPM to quantify the aleatoric uncertainty caused by evidence layers (Lisitsin et al., 2014; Wang et al., 2020; Gao et al., 2024). Further, a workflow based on Monte Carlo simulations, coupled with global sensitivity analysis, was developed by Wang and Zuo (2023) to mitigate uncertainties associated with geochemical anomalies. Additionally, Yang et al. (2023) introduced a hybrid model combining the direct sampling algorithm and convolutional neural network to quantify the uncertainty of evidence layers for MPM. Regarding epistemic uncertainty in MPM, Zhang et al. (2022) utilized Bayesian logistic regression quantify epistemic uncertainty. Yousefi et al. (2024) proposed the use of majority voting and confidence index methodologies to reduce epistemic uncertainty. Moreover, Huang et al. (2022) utilized Bayesian convolutional neural net-

work quantify aleatoric and epistemic uncertainties in geochemical anomalies mapping. Despite these developments, there are limited studies on the joint quantification of aleatoric and epistemic uncertainties in 3D MPM. Ignoring either aleatoric or epistemic uncertainty can lead to biased decision-making. A better understanding of the limitations in 3D geological modeling, and predictive model parameters and hyperparameters can be achieved by considering aleatoric and epistemic uncertainties. This is beneficial for exploration decision-making. Furthermore, the most commonly used performance (e.g., AUC) and target determining [e.g., prediction-area, (P-A) plot] metrics focus primarily on accuracy and predictive probabilities, with less consideration given to uncertainty. To the best of our knowledge, only the return-risk analysis proposed by Wang et al. (2020) determines exploration targets with low uncertainty and high accuracy. Therefore, it is essential to develop joint uncertainty-accuracy metrics.

This study proposes an uncertainty-quantification ML framework for 3D MPM. The proposed framework consists of three parts: (1) uncertainty-quantification random forest (UQRF) for 3D MPM as well as for aleatoric and epistemic uncertainties quantification; (2) Bayesian hyperparameter optimization to tune hyperparameters automatically for the UQRF modeling; and (3) joint uncertainty-accuracy metrics, namely accuracy-rejection curve to provide a quantitative probability and uncertainty threshold for outlining of exploration targets. In this study, we emphasize that aleatoric uncertainty is mainly related to evidence layers, primarily influenced by uncertainties in 3D geological modeling. This includes two key aspects: (1) the complexity of the geometry and the lithological heterogeneity of a 3D geological model and (2) the amount of information available in a 3D geological model. Meanwhile, the epistemic uncertainty observed is tied to the variability of algorithm parameters. We conducted a case study in the Wulong gold district to prove the novelty and practicality of our proposed framework for 3D MPM.

## GEOLOGICAL BACKGROUND

The Wulong gold district lies along the southeastern margin of the Liaodong Peninsula on the North China Craton (Fig. 1a) (Yu et al., 2018; Du et al., 2023; Feng et al., 2023). It is the largest gold district in the Liaodong Peninsula, boasting over 135

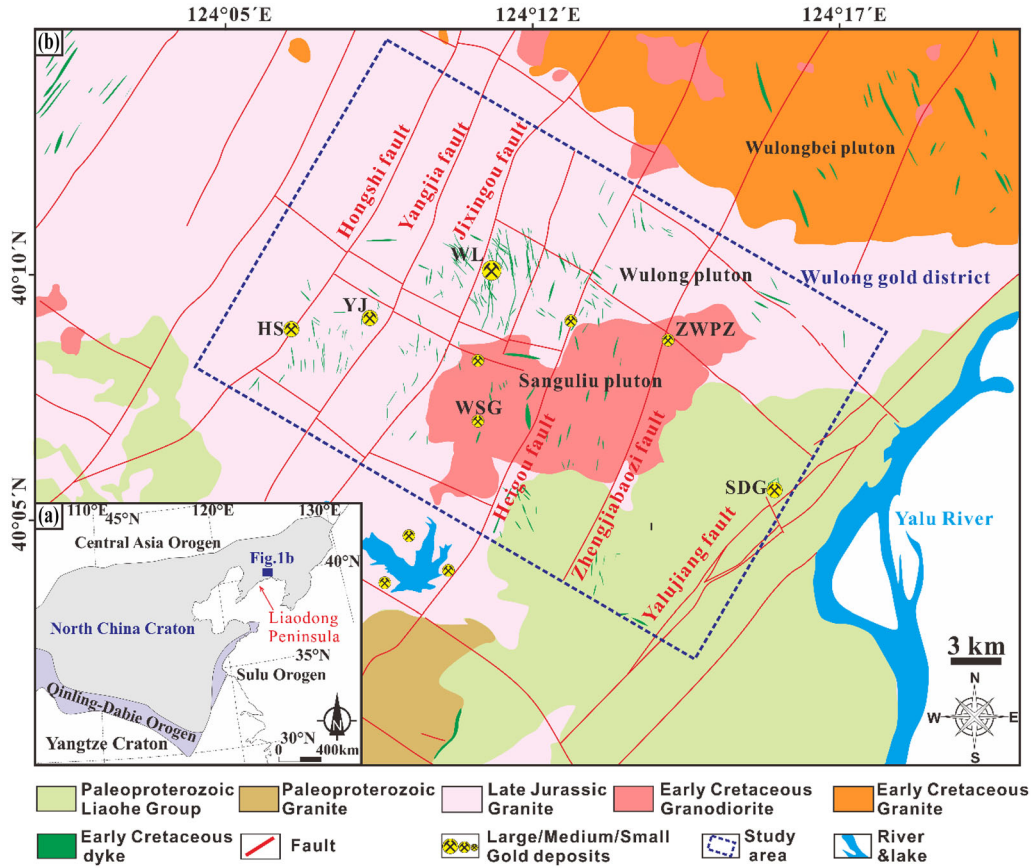


**Figure 1.** (a) Simplified geotectonic map of the North China Craton. (b) Simplified geological map of the Wulong Au district. WL, YJ, SDG, HS, WSG, and ZWPZ are the Wulong, Yangjia, Sidaogou, Hongshi, Weishagou, and Zhengwapuzi gold deposits, respectively (modified from Zhang et al., 2019; Yu et al., 2020).

tons of mined and remaining non-JORC gold resources (Yu et al., 2018; Zhang et al., 2022). Widespread outcrops of Mesozoic intrusions characterize the study area (Fig. 1b). The Paleoproterozoic Liaohu Group, comprising a series of metamorphosed volcanic–sedimentary rocks, is distributed along the southeastern margin of the Wulong gold district (Fig. 1b) (Liu et al., 2019; Zhang et al., 2020a). Paleoproterozoic granite, which forms the basement rocks, is exposed in the southern periphery of the Wulong gold district. The Late Jurassic granite (Wulong pluton) was dated using zircon U–Pb dating to be 163–155 Ma (Wu et al., 2005; Yu et al., 2020; Zhang et al., 2020a). Zircon U–Pb dating unveiled that the Early Cretaceous granodiorite (Sanguli pluton) emplaced simultaneously during 132–126 Ma (Fig. 1b) (Wei et al., 2003; Yu et al., 2018). The Early Cretaceous dykes (mostly diorite and lamprophyre) were 127–113 Ma via zircon U–Pb dating (Liu et al., 2019). Dating of gold-related

minerals by Rb–Sr and U–Pb methods indicated that the gold mineralization in the Wulong gold district occurred at 125–115 Ma, and thus coeval with the Early Cretaceous intrusions (Wu et al., 2005; Liu et al., 2019; Yu et al., 2020; Zhang et al., 2020a). Studies of isotopes (e.g., S, Pb, He, and Ar in pyrite, and H and O in quartz) revealed that the ore-forming fluid for gold mineralization is mainly derived from magma (Yu et al., 2018; 2020; Liu et al., 2019; Zhang et al., 2020a; Feng et al., 2023). There are district-scale subparallel NE–NNE-striking faults (including Hongshi, Yangjia, Jixingou, Heigou, and Zhengjiabaozi) from west to east of the Wulong gold district (Fig. 1b). These NE–NNE-striking faults were subsidiary faults of the regional-scale Yalujiang fault to the southeast of the study area (Zhang et al., 2020b; Du et al., 2023). Potential field, magnetotelluric (MT), and seismic surveys revealed district-scale subsurface NW-striking faults in the Wulong gold district (Zhang et al., 2019; Zheng



et al., 2022). The study area primarily consists of the large vein-type Wulong gold deposit (non-JORC gold resources > 80 t, with grades of 2.9–19.8 g/t), the medium vein-type Yangjia gold deposit (non-JORC gold resources > 20 t, with grades of 2.8–14.9 g/t), the medium disseminated Sidaogou gold deposit (non-JORC gold resources > 11 t, with grades of 2.9–14.9 g/t) (Fig. 1b) (Zhang et al., 2022). Additionally, there are small vein-type gold deposits, including Hongshi, Weishagou, and Zhengwapuzi (Fig. 1b). Excluding the Sidaogou gold deposit, all the other known gold deposits in the district are hosted within Mesozoic intrusions (Fig. 1b) (Zhang et al., 2022; Feng et al., 2023). Most gold deposits are spatially controlled by NE–NNE-striking faults (Fig. 1b) (Zhang et al., 2019; Du et al., 2023). However, some orebodies (e.g., the V163 orebody of the Wulong gold deposit) are also hosted in NW-striking faults (Yu et al., 2018; Zhang et al., 2020a). Some Early Cretaceous dykes and the orebodies occupy the same fault system. The ore-forming fluid released from the intrusions ascended along NE–NNE- and NW-striking faults and mineralized in the suitable traps (Zhang et al., 2020a; Du et al., 2023). In summary, previous geological, geochemical, geochronological, and geophysical studies indicated that the mineral system in the Wulong gold district hosts an intrusion-related gold mineral system (IRGS) related to Early Cretaceous intrusions (Yu et al., 2018; Zhang et al., 2019, 2020a; Feng et al., 2023).

### 3D GEOLOGICAL MODELING AND EVIDENCE LAYERS

The Mponeng gold deposit in the Gauteng province of South Africa is one of the deepest operating deposits globally, with approximately 4 km mining depth (Manzi et al., 2015). With the development of mining technology, the ability to mine gold 5 km in the subsurface is likely in the future. Therefore, in this study, the depth of 3D geological modeling and MPM was set to 5 km.

This study utilized SKUA-GOCAD software to construct a 3D geological model. The cell size of the 3D geological model was set to  $50 \times 50 \times 50$  m based on the minimum geological body size and computing power. The sets of geoscience data used for building the 3D district-scale geological model

are enumerated in Table 1. Typically, the 3D district-scale geological model was built using geological and geophysical data (Fig. 2a) (Malehmir et al., 2009; Lü et al., 2013; Wang et al., 2015; Zhang et al., 2019).

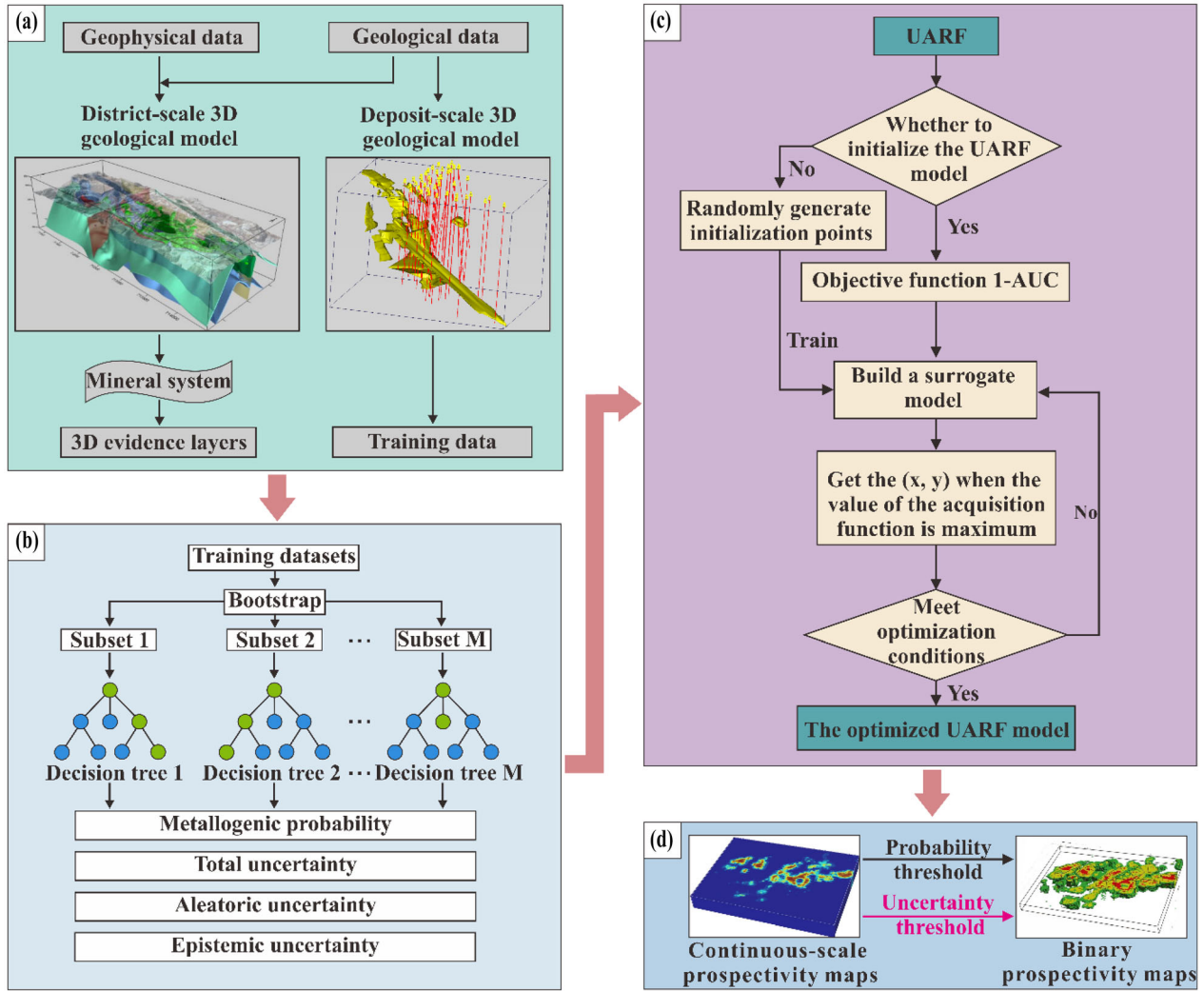
The petrophysical properties of lithologies in the study area are listed in Table 2. The Bouguer gravity anomalies and reduced-to-pole (RTP) magnetic anomalies are influenced by variations in density and magnetic susceptibility of geological units at different depths in the subsurface (Anderson et al., 2017). Therefore, before performing potential field inversions, it is necessary to distinguish the shallow residual (subsurface) gravity and RTP magnetic anomalies from the superimposed gravity and magnetic anomalies (Li & Oldenburg, 1996; 1998). This study made use of the residual gravity and RTP magnetic anomalies for inversion derived by Zhang et al. (2019) (Fig. 3). UBC-GIF software was employed to perform the 3D potential field inversions. The MT survey lines are shown in Figure 3. The MT inversion was performed by the China Geological Survey using the REBOCC method via *Winglink*. In the 3D potential field and MT inversions, the study area was partitioned into  $50 \times 50 \times 50$  m meshes, consistent with the cell size of the 3D geological model. The 3D gravity, magnetic, and MT inversion models are shown in Figure 4. The detailed process of constructing the 3D district-scale geological model via geological and geophysical data can be found in Zhang et al. (2019, 2021b, 2022).

The final 3D district-scale geological model is shown in Figure 5. The model of Early Cretaceous granodiorite and dyke (representing heat and fluid sources), the model of NE–ENE-striking faults (representing pathways and traps), and the model of NW-striking faults (representing pathways and traps) were selected to generate the evidence layers by buffer technique (Fig. 5). The geophysical evidence layers were derived via the potential field and MT inversions (Fig. 4).

The sets of geoscience data used for building the 3D deposit-scale geological model are enumerated in Table 3. The 3D orebody models of the large Wulong, medium Yangjia, and medium Sidaogou gold deposits are shown in Figure 6, and they served as positive training samples. The 3D non-mineralization voxels from the mine plans and drill holes were utilized as negative training samples (Xiang

**Table 1.** Geoscience datasets for 3D district-scale geological modeling

Data	Description
Geological map	1:50,000-scale geologic map; strike/dip measurements of surface structural elements; 1:5000-scale geological profiles located at the same position as the MT profiles
Petrophysical data	The density, apparent magnetic susceptibility, and resistivity were measured from 866 rocks and orebody samples
Bouguer gravity data	Acquired with average spacing of $\sim 500$ m, the grid of gravity contour plans was $500 \text{ m} \times 500 \text{ m}$ . The Bouguer correction parameters were reduction density of $2670 \text{ kg/m}^3$ and terrain corrections of 20 km (IGF 1980)
RTP magnetic data	Acquired with average spacing of $\sim 250$ m, the grid of magnetic contour plans was $250 \text{ m} \times 250 \text{ m}$ . The RTP parameters were the geomagnetic field declination $-8.6^\circ$ , inclination $57.93^\circ$ (IGRF 2010)
MT data	Acquired with average spacing of $\sim 500$ m and the investigation depth was ca. 5000 m

**Figure 2.** Workflow of the proposed uncertainty-quantification machine learning framework.

## An Uncertainty-Quantification Machine Learning Framework for Data-Driven

**Table 2.** Petrophysical properties of geological units in the study area

Geological units	Density (g/cm <sup>3</sup> )	Magnetic Susceptibility ( $\times 10^{-6}$ SI)	Resistivity (log <sub>10</sub> $\Omega$ m)
Paleoproterozoic Liaohe Group	2.78–2.83	100–180	3.17–3.37
Paleoproterozoic granite	2.51–2.64	100–220	3.36–3.47
Jurassic granite	2.46–2.62	20–180	3.34–3.41
Early Cretaceous granite	2.46–2.62	80–200	3.34–3.41
Early Cretaceous granodiorite	2.65–2.75	201–286	3.39–3.53
Early Cretaceous dyke	2.69–2.85	278–403	3.38–3.54

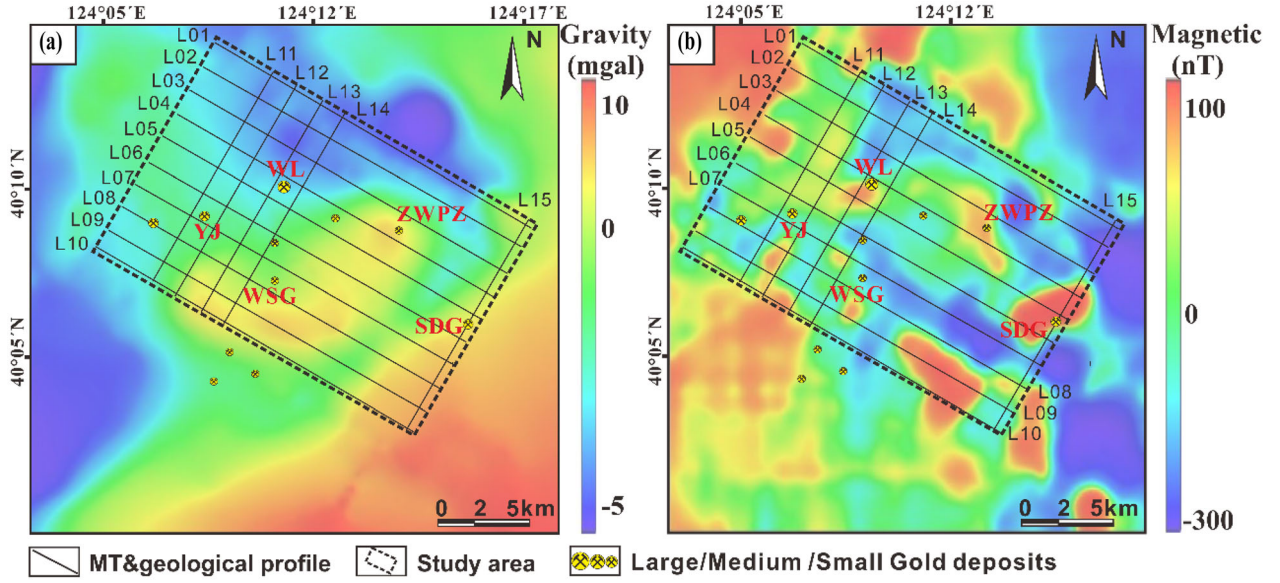


**Figure 3.** (a) Residual gravity anomalies and (b) RTP magnetic anomalies.

et al., 2020; Li et al., 2023). The number of positive and negative training samples were 4101 and 10, 560, respectively.

## METHODOLOGY

### Uncertainty-Quantification Random Forest

RF is a bootstrap aggregating (bagging)-based ensemble learning algorithm that is employed extensively in spatial geoscience modeling, including MPM, lithological mapping, and landslide susceptibility mapping (Carranza & Laborte, 2015; Harris et al., 2015; Zhou et al., 2021). The base learner of the RF is the classification and regression tree (CART) (Fig. 2b). Let  $H = \{h_1, h_2, \dots, h_M\}$  be an ensemble model in the form of a RF consisting of

CART ( $h_i$ ). Given a query instance  $x$ , the classification probability yielded by the  $h_i$  can be expressed as Breiman (2001):

$$p(y|h_i, x) = \frac{n_{ij}(y)}{n_{ij}}, \quad i = 1, 2, \dots, M, \quad j = 1, 2, \dots, N \quad (1)$$

where  $n_{ij}(y)$  is the number of training instances in the leaf node ( $R_{ij}$ ) that belongs to class  $y$ , and  $n_{ij}$  is the total number of training instances in the leaf node (sum of instances of all classes  $Y$ ) (Breiman, 2001). Mathematically, the final classification probability ( $p_{forest}$ ) produced by RF is calculated by averaging  $p(y|h_i, x)$  as Breiman (2001):

$$p_{forest} = \frac{1}{M} \sum_{m=1}^M p(y|h_i, x), \quad i = 1, 2, \dots, M. \quad (2)$$

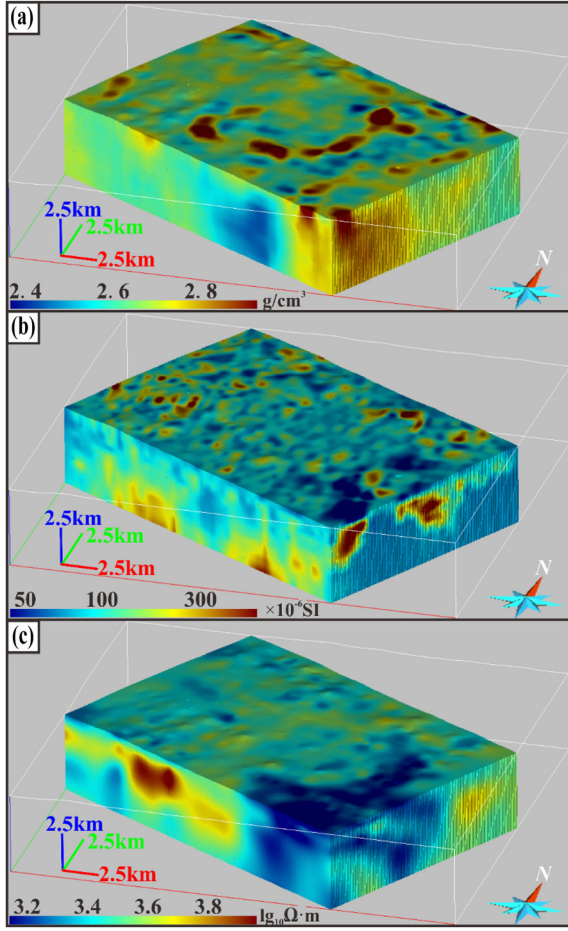


Figure 4. 3D gravity, magnetic, and MT inversion models.

The RF can provide class probabilities as outputs, but it does not provide a measure of uncertainty associated with those probabilities. Thus, this study introduced the UQRF to quantify total uncertainty ( $u_t(x)$ ) by entropy as Shaker and Hüllermeier (2020), Zhang et al. (2023a, b):

$$u_t(x) = - \sum_{y \in Y} \left( \frac{1}{M} \sum_{i=1}^M p_L(y|h_i, x) \right) \log_2 \left( \frac{1}{M} \sum_{i=1}^M p_L(y|h_i, x) \right) \quad (3)$$

where  $p_L(y|h_i, x) = \frac{n_{ij}(y)+1}{n_{ij}+|Y|}$  is the improved Eq. (1) by Laplace-corrected relative frequencies, which can address the problem of zero probabilities in prediction (Shaker & Hüllermeier, 2020);  $|Y|$  is the number of predicted categories, and in this study,  $|Y| = 2$ . The hyperparameters of each CART in the RF are consistent, and so the differences in predic-

tions made by each CART are primarily due to the training data. Entropy can describe the uncertainty of the various probability distributions predicted by each CART (Hüllermeier & Waegeman, 2021). Therefore, aleatoric uncertainty ( $u_a(x)$ ) of an UQRF model can be calculated by the entropy of each CART in the model (Eq. 4) (Shaker & Hüllermeier, 2020; Zhang et al., 2023a, b), thus:

$$u_a(x) = - \frac{1}{M} \sum_{i=1}^M \sum_{y \in Y} p_L(y|h_i, x) \log_2 p_L(y|h_i, x) \quad (4)$$

The epistemic uncertainty ( $u_e(x)$ ) can be calculated as  $u_e(x) = u_t(x) - u_a(x)$ . When calculating the classification probabilities of UQRF, the  $p(y|h_i, x)$  in Eqs. 1 and 2 needs to be replaced with  $p_L(y|h_i, x)$  (Shaker & Hüllermeier, 2020; Zhang et al., 2023a, b).

### Bayesian Hyperparameter Optimization

Bayesian hyperparameter optimization is a probabilistic model-based technique employed for automatically tuning the hyperparameters of ML models (Bergstra et al., 2013). It aims to obtain optimal hyperparameters automatically while avoiding the significant computational time wasted by traditional hyperparameter optimization methods (e.g., grid search and random search) (Zhang et al., 2023a, b). Bayesian hyperparameter optimization consists of two fundamental parts: the surrogate model and the acquisition function (Fig. 2c) (Zhang et al., 2021a). The surrogate model estimates the distribution of the objective function, providing potential well-performed hyperparameters. This study utilized the tree-structured Parzen estimator (TPE) as the surrogate model. Mathematically, the TPE can be represented as Zhang et al. (2021a):

$$p(\lambda|\varphi) = \begin{cases} l(\lambda) & \text{if } \varphi < \varphi^* \\ g(\lambda) & \text{if } \varphi \geq \varphi^* \end{cases} \quad (5)$$

where  $p(\lambda|\varphi)$  represents the conditional probability of the hyperparameters combination ( $\lambda$ ) and the model objective function ( $\varphi$ );  $\varphi^*$  is the threshold of  $\varphi$ .

The acquisition function guides the search for the next hyperparameters to evaluate based on the current surrogate model. This study utilized the expected improvement (EI) as acquisition function.



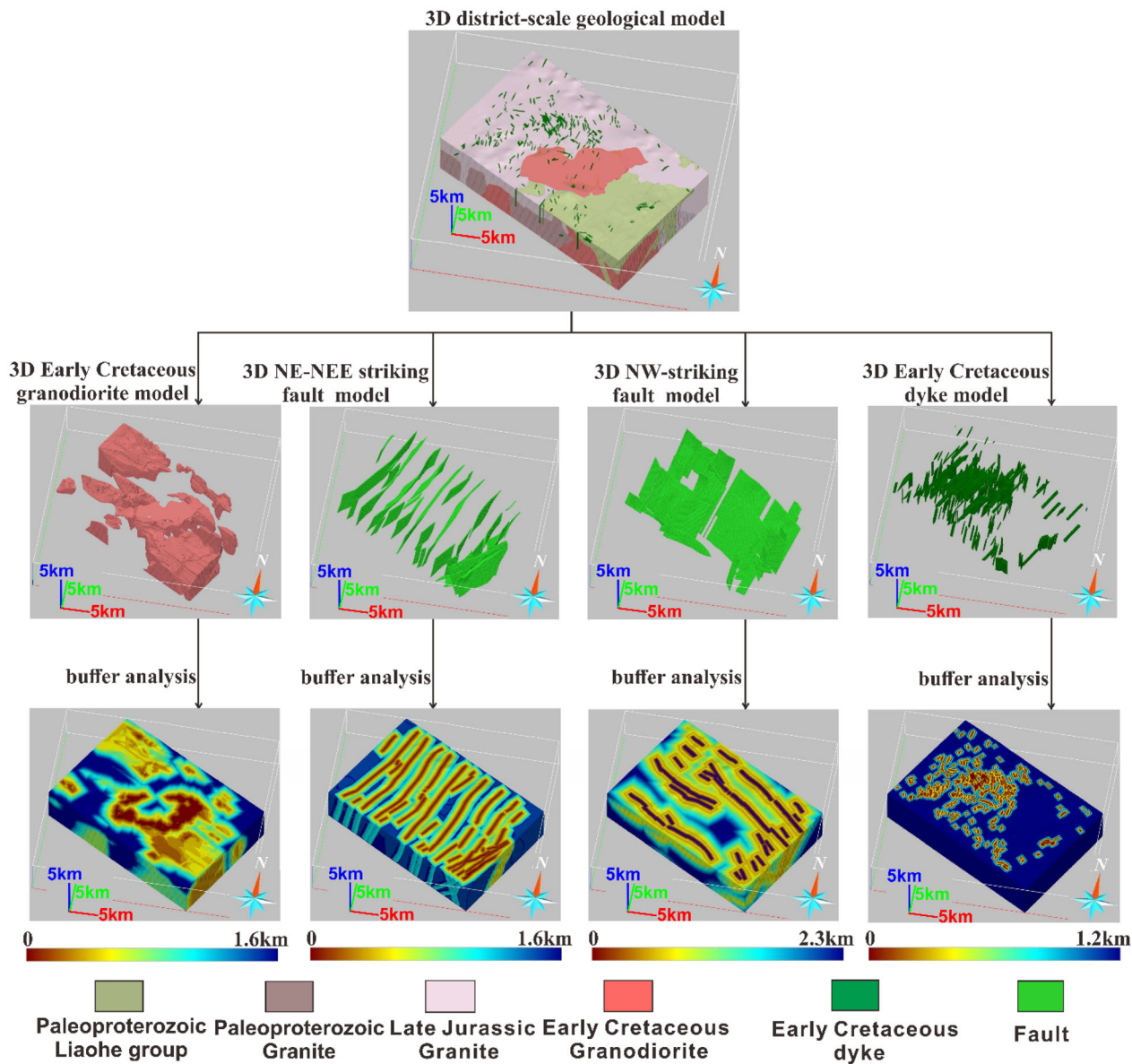
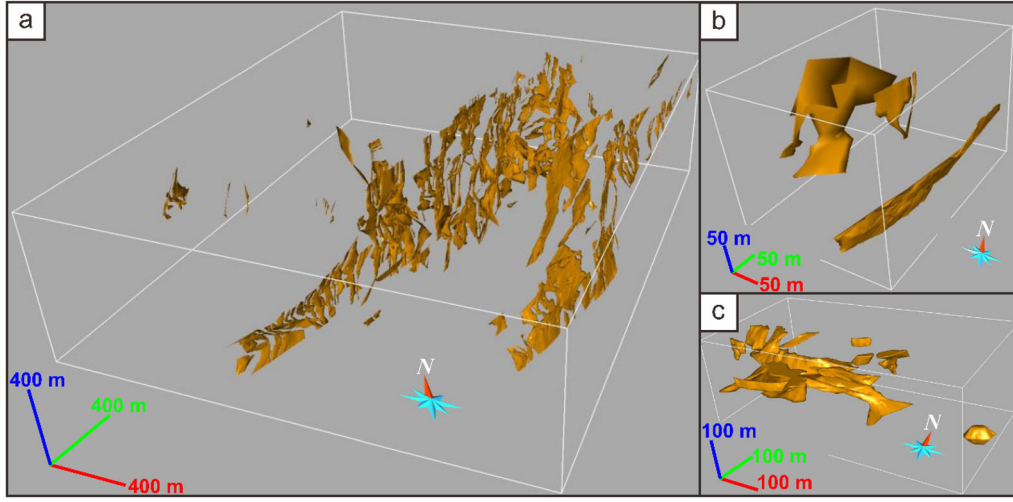


Figure 5. 3D district-scale geological and evidence layers models.

Table 3. Geoscience datasets for 3D orebody modeling

Gold deposits	Data	Number	Source
Wulong	1:500-scale geological profiles	20	Liaoning Wulong gold mining Co., Ltd
	1:100-scale mine plans	40	
Yangjia	1:100-scale mine plans	5	Liaoning geological bureau of non-ferrous
Sidaogou	Drill holes with average depth of ~ 200 m	10	
	1:500-scale geological profiles	18	
	1:100-scale mine plans	8	



**Figure 6.** 3D orebody models of the (a) Wulong, (b) Yangjia, and (c) Sidaogou gold deposits.

Mathematically, the  $EI_{\varphi^*}$  can be represented as Zhang et al. (2021b):

$$EI_{\varphi^*} = \frac{\gamma\varphi * l(\lambda) - l(\lambda) \int_{-\infty}^{\varphi^*} p(\varphi) d\varphi}{\gamma l(\lambda) + (1 - \gamma)g(\lambda)} \propto \left( \gamma + \frac{g(\lambda)}{l(\lambda)} (1 - \gamma) \right)^{-1} \quad (6)$$

The Bayesian hyperparameter optimization process begins with an initial model (Fig. 2c) (Bergstra et al., 2013). Next, the objective function of the ML model is defined and utilized to construct the surrogate model (Fig. 2c) (Bergstra et al., 2013). The acquisition function then recommends the next hyperparameters to be evaluated (Fig. 2c) (Bergstra et al., 2013). This iterative process continues until the optimal hyperparameters are obtained or a predefined number of iterations is reached (Zhang et al., 2021b) (Fig. 2c).

### Accuracy-Rejection Curve

In 3D MPM, the outputs of most ML models are continuous-probability prospectivity maps. However, binary prospectivity maps could be more intuitive for exploration than continuous-probability prospectivity maps because the former show results as exploration targets and background (Fig. 2d) (Porwal et al., 2010). Most binary prospectivity mapping methods [e.g., prediction-area (P-A) plot, capture-efficiency curves, and concentration-vol-

ume fractal curves] are predominantly factored in probability while neglecting uncertainty (Porwal et al., 2010; Yousefi & Carranza, 2015; Li et al., 2016). This affects the reliability of 3D MPM in guiding exploration (Wang et al., 2020). Furthermore, aleatoric uncertainty and epistemic uncertainty influence the accuracy and stability of a ML model (Senge et al., 2014; Yong & Brintrup, 2022).

Previous studies have indicated that permitting the abstention from classified results whose uncertainty surpasses a specific threshold can lead to enhanced classification accuracy (Senge et al., 2014; Yong & Brintrup, 2022). Therefore, this study introduced the accuracy-rejection curve for determining exploration targets and background. The x-axis of the accuracy-rejection curve represents the rejection rate, which indicates the percentage of classified instances exceeding an uncertainty threshold out of the total classified instances (Senge et al., 2014). The y-axis of the accuracy-rejection curve represents the accuracy at that specific rejection rate (Senge et al., 2014). As the uncertainty threshold reduces, both the rejection rate and accuracy increase. Similar to using the capture-efficiency curve (Porwal et al., 2010), exploration targets and background can be separated by varying slopes of the accuracy-rejection curve (Senge et al., 2014). Compared to the return-risk analysis (Wang et al., 2020; Zhang et al., 2022), the accuracy-rejection curve can provide a quantifiable uncertainty threshold for binary prospectivity mapping.

## RESULTS AND DISCUSSION

### 3D Probability Prospectivity Map

The data imbalance issue in this study has minimal impact on RF-based models (Carranza & Laborte., 2015; Lindsay et al., 2022). The RF and UQRF models were implemented under JupyterLab and trained on a Dell Precision 5530 computer with a Core i7 2.60 GHz processor, 16.00 GB of RAM, and a 1 TB hard drive. The critical hyperparameters space of the RF and UARF are listed in Table 4. The results obtained by RF in this study can be viewed as a deterministic case study. In contrast, those obtained by UQRF may be regarded as an uncertainty-quantification case study. This distinction allows for a comparative analysis between deterministic and uncertainty-based approaches. The results of the fivefold cross-validation are listed in Table 5. The optimal hyperparameters of the best-performing RF (Fold 4) and UQRF (Fold 1) models are listed in Table 4. The 3D probability prospectivity maps obtained by the RF and UQRF models are shown in Figure 7. According to the AUC values, the UARF model demonstrated comparable performance to the RF model (Table 5), confirming that improvements made by incorporating Laplace-corrected relative frequencies into UQRF do not impact its predictive performance. Among these evidence layers, the Early Cretaceous granodiorite

model, representing the heat and fluid source component of mineralization, was the most statistically significant in both the RF and UQRF models (Table 6), thus supporting the hypothesis that the mineral system of the study area is IRGS.

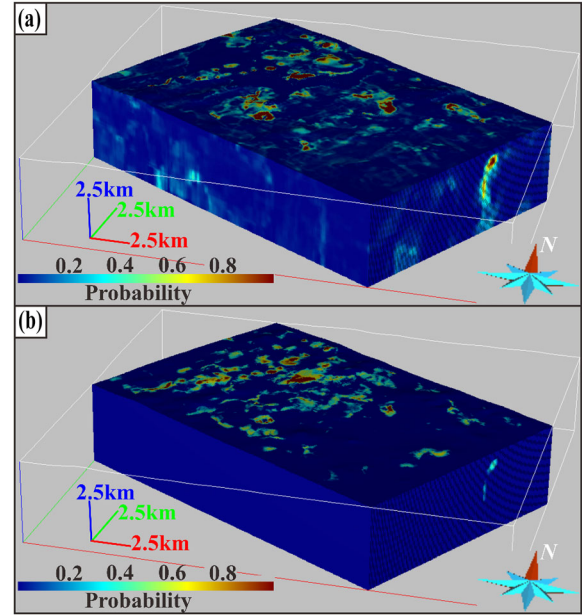


**Figure 7.** 3D probability prospectivity maps obtained by the (a) RF and (b) UQRF models..

**Table 4.** Hyperparameters of the best-performing RF and UQRF models

Hyperparameters	Hyperparameters space	Optimal hyperparameters of RF	Optimal hyperparameters of UQRF
n_estimators	[1... 300]	50	72
max_depth	[2... 20]	12	14
min_samples_split	[2... 20]	2	3
min_sample_leaf	[1...20]	2	4

**Table 5.** AUC and average AUC in fivefold cross-validation

Data	Classification algorithm	Fold 1	Fold 2	Fold 3	Fold 4	Fold 5	Average AUC
Training data	RF	0.91	0.89	0.90	<b>0.92</b>	0.91	0.91
	UQRF	<b>0.92</b>	0.90	0.89	0.91	0.91	0.91
Testing data	RF	0.92	0.91	0.90	<b>0.93</b>	0.91	0.91
	UQRF	<b>0.93</b>	0.91	0.90	0.91	0.91	0.91

The bold in Table indicates the best performing prediction models

**Table 6.** Feature importance of evidence layers to 3D prospectivity mapping

Predictive models	Early Cretaceous granodiorite model	NE-striking faults model	NW-striking faults model	Early Cretaceous dyke model	Density model	Magnetic susceptibility model	Resistivity model
RF	<b>0.258</b>	0.198	0.023	0.101	0.213	0.038	0.098
UQRF	<b>0.286</b>	0.163	0.036	0.151	0.183	0.021	0.091

The bold in Table indicates the most critical evidence layer for prediction models

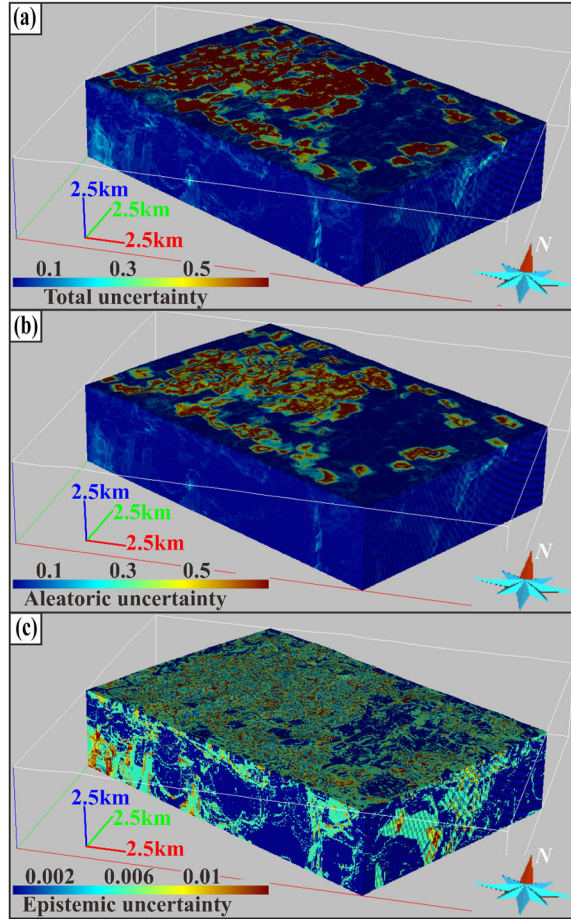


**Figure 8.** 3D (a) total, (b) aleatoric, and (c) epistemic uncertainties prospectivity maps.

### 3D Uncertainty Prospectivity Map

The 3D total, aleatoric, and epistemic uncertainties prospectivity maps obtained by the UQRF model are shown in Figure 8. The aleatoric uncertainty (varying from 0 to 1) greatly surpassed the epistemic uncertainty (varying from 0 to 0.012), making it a substantial contributor to the total

uncertainty (varying from 0 to 1) (Fig. 8). The low epistemic uncertainty obtained indicates that the UQRF model can capture effectively the underlying ore-forming patterns present in the evidence layers. Sensitivity analysis can be used to analyze the contribution of evidence layers to aleatoric uncertainty (Wang and Zuo, 2023). This study conducted a sensitivity analysis focusing on the impact of evidence layers on aleatoric uncertainty, as measured by total Sobol indices, which revealed that the Early Cretaceous dyke had the largest contribution (Fig. 9). The high aleatoric uncertainty is also spatially associated with the Early Cretaceous dyke model (Fig. 10). Compared to other geological objects, the Early Cretaceous dyke is distinguished by its small size and intricate geometry. These characteristics make it particularly difficult to detect the Early Cretaceous dyke in geophysical data. Consequently, models of the Early Cretaceous dyke are marked by a higher degree of uncertainty compared to the other geological units.

The 3D aleatoric uncertainty prospectivity map obtained by the UQRF model has the potential to capture the uncertain object of the 3D geological model. In order to further compare the disparities between aleatoric and epistemic uncertainties in 3D MPM, we created a series of training datasets of varying sizes. Each training dataset comprises five sets of training data, each randomly sampled from the total training dataset at the same size. In other words, each training dataset contained five sets of training data with the same size but not entirely identical instances. Correspondingly, the test dataset also comprised five sets of testing data with the same size but not entirely identical instances. The epistemic and aleatoric uncertainties obtained by the UQRF model on each testing dataset were the averages of these five sets of testing data. The critical hyperparameters of each model were tuned by the Bayesian hyperparameter optimization. Figure 11 illustrates the results regarding the average aleatoric and epistemic uncertainties as a function of training data size. The aleatoric uncertainty fluctu-



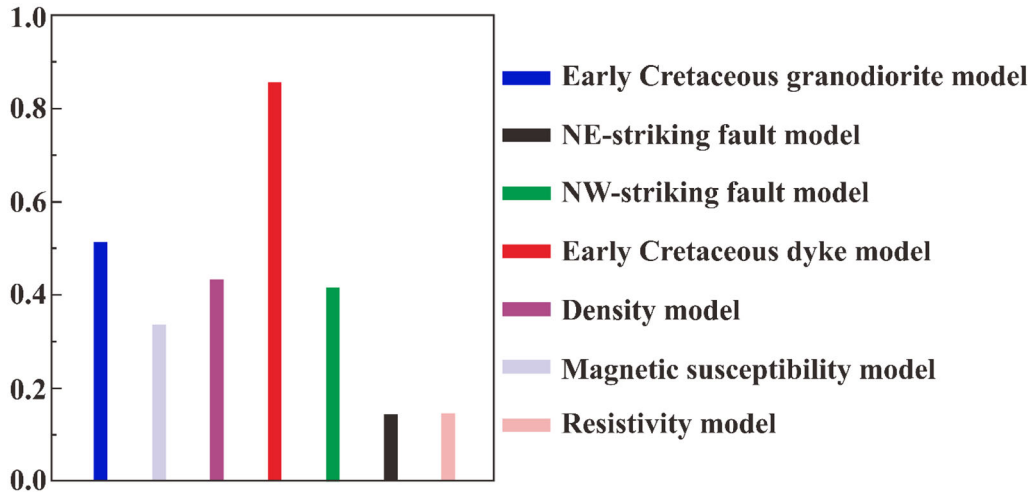


**Figure 9.** Sensitivity analysis of evidence layers to aleatoric uncertainty by total Sobol indices.

ated as the size of the training dataset increased, whereas the epistemic uncertainty decreased with increase in the size of the training dataset (Fig. 11). As mentioned above, aleatoric uncertainty constitutes a significant portion of the total uncertainty of 3D MPM. The observed variations in aleatoric uncertainty for each random sampling can be linked to the varying levels of inherent noise in the selected data subsets during each instance. For instance, training sets with fewer data points related to the Early Cretaceous dyke model may exhibit lower aleatoric uncertainty. In this study, increasing the collection of deposit-scale mine plans and drill hole data to generate more training data had a limited impact on reducing the total uncertainty of the 3D MPM. Improving the quality of the Early Cretaceous dyke modeling had a more significant effect on reducing the total uncertainty of 3D MPM.

## Mapping of 3D Exploration Targets

This study determined exploration targets using probability and uncertainty. Compared to merely relying on predictive probabilities to delineate targets, incorporating uncertainty allows for further focusing on areas with high predictive probabilities and low uncertainty, potentially enhancing the success rate of subsurface exploration. Firstly, the commonly employed P–A plot was utilized to determine exploration targets based on probability. The x-value at the intersection point within the P–A

plot served as a threshold of probability for outlining exploration targets (Fig. 12 and Table 7). In the P–A plot, a prospectivity model with a higher intersection point compared to another prospectivity model indicates that it performed better. The P–A plot indicates that the UQRF model slightly outperformed the RF model (Fig. 12, Table 7). The exploration targets determined by the P–A plots for the RF and UQRF models are shown in Figure 14a, b, respectively. Secondly, the accuracy–rejection curve, considering uncertainty, was used to further determine the exploration targets for the UQRF model. The x-value at the changing slope portion within the accuracy–rejection curve served as a threshold of uncertainty for delineating potential exploration targets (Fig. 13). The exploration targets for the UQRF model based on both the P–A plot and accuracy–rejection curve are shown in Figure 14c. The exploration targets obtained from the UQRF model were distributed primarily around the Wulong and Yangjia gold deposits, as well as the Jixingou and Yangjia faults (Fig. 14c). There were fewer exploration targets in the vicinity of the Sidaogou gold deposit (Fig. 14c). As mentioned above, aside from the Sidaogou gold deposit, all known gold deposits in the area are situated within Mesozoic intrusions (Fig. 1b). The 3D uncertainty model and targeting results indicated that the Sidaogou gold deposit might have a different ore-forming process compared to the other deposits in the study area. Therefore, based on the aleatoric uncertainty modeling and sensitivity analysis, we

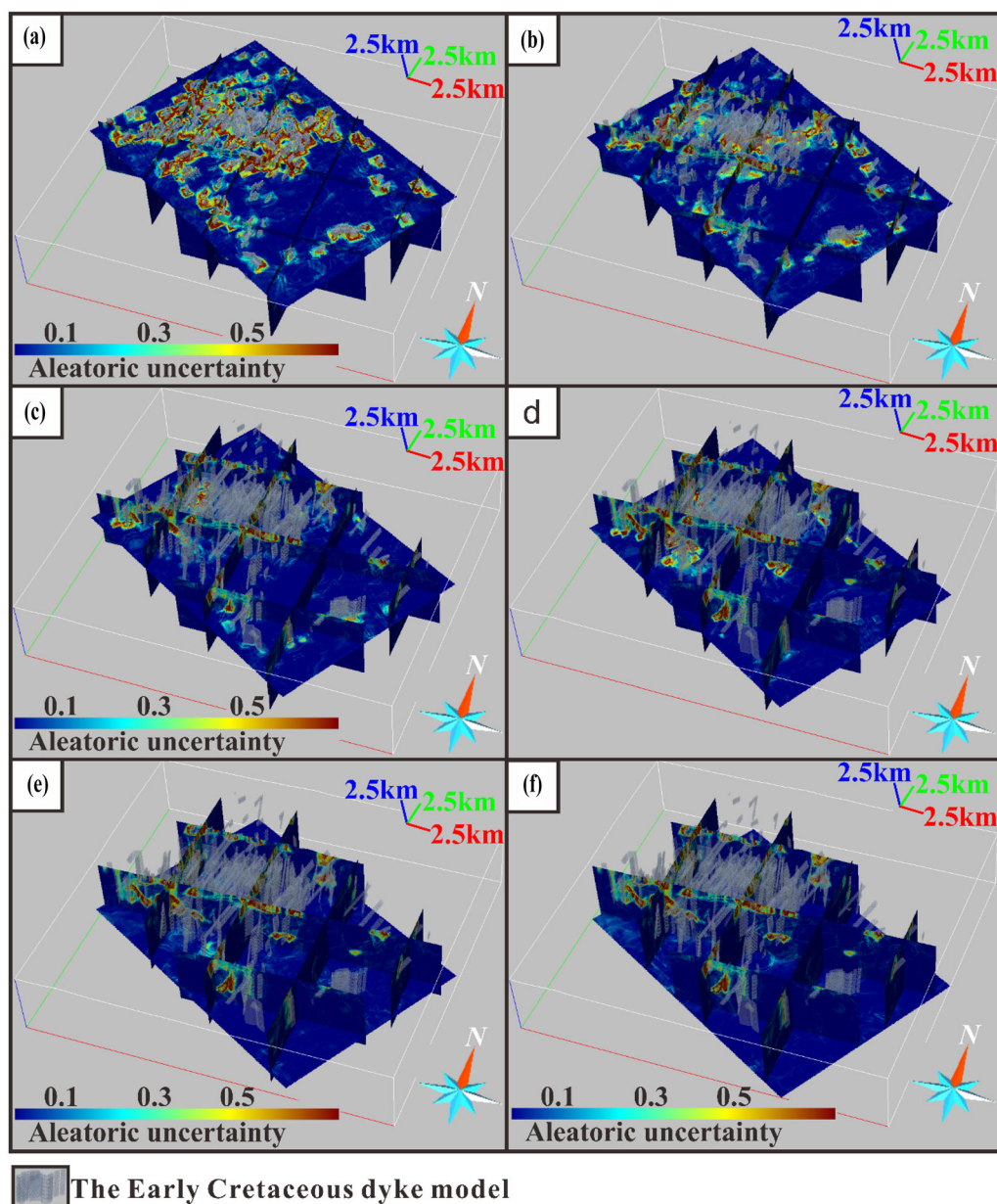


**Figure 10.** (a)–(f) are the 2D aleatoric uncertainty mapping cross profiles at – 500 m, – 1000 m, – 2000 m, – 3000 m, – 4000 m, – 5000 m, respectively.

suggest paying attention to the spatial distribution of the Early Cretaceous dyke in further investigation of the obtained exploration targets.

## CONCLUSIONS

Mineral system conceptual model, aleatoric, and epistemic uncertainties impact 3D MPM and

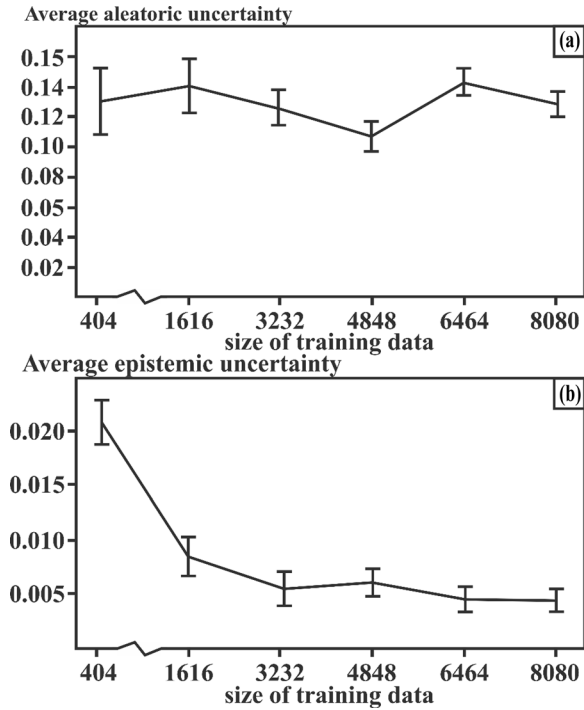


**Figure 11.** Average (a) aleatoric uncertainty and (b) epistemic uncertainty for the UQRF model as a function of training data size.

exploration targeting. This study proposes an uncertainty-quantification ML framework consisting of the UQRF, Bayesian hyperparameter optimization, and accuracy-rejection curve. The UQRF can conduct MPM and, at the same time, quantify aleatoric uncertainty and epistemic uncertainty. Bayesian hyperparameter optimization is utilized for hyperparameter tuning of the UQRF modeling. The P-A plot and accuracy-rejection curve are utilized further to determine exploration targets based on probability and uncertainty. The case study demonstrated that our proposed uncertainty-quantification ML framework enables the construction of both 3D probability prospectivity maps and 3D

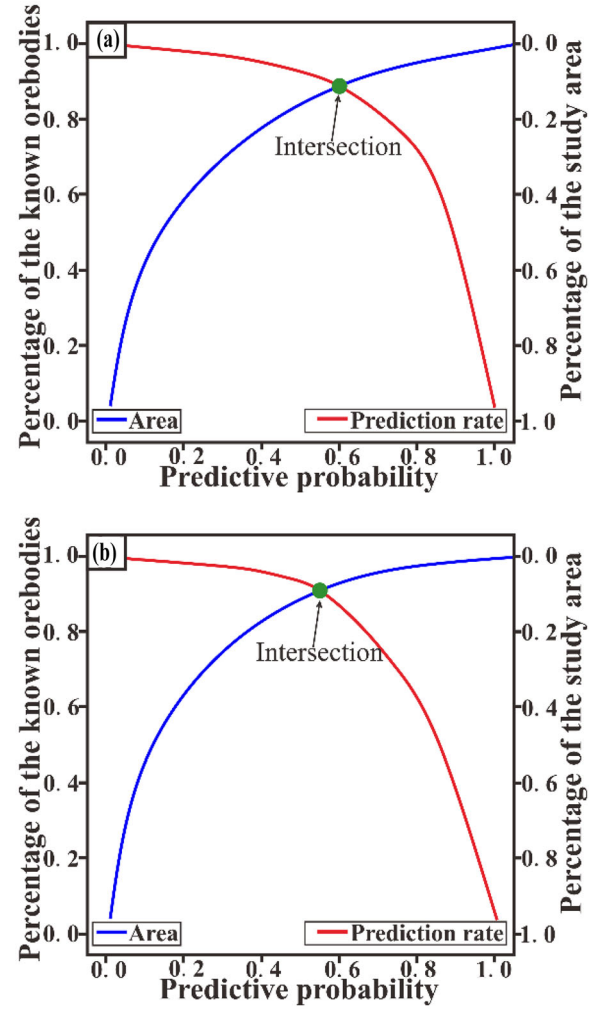


**Figure 12.** P-A plots of the (a) RF model and (b) UQRF model.

uncertainty prospectivity maps. The aleatoric uncertainty is a valuable index for assessing the quality of a 3D geological model for 3D MPM. For future studies, our primary focus will be to reduce uncertainty within the 3D MPM process via ML.

**Table 7.** Parameters in the P-A plots of the RF and UQRF models

Predictive models	RF model	UQRF model
Threshold for determining the targets	0.59	0.54
Percentage of study area occupied by the targets	11%	9%
Percentage of known orebody occupied by targets	89%	91%

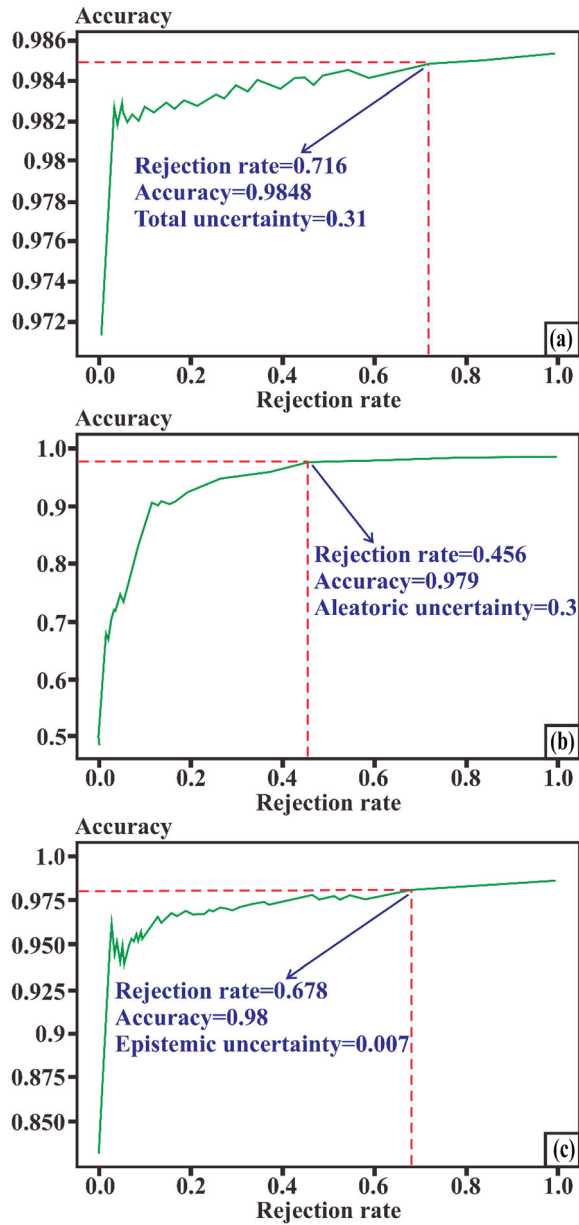


**Figure 13.** Accuracy–rejection curves of **a** total uncertainty, **b** aleatoric uncertainty and **c** epistemic uncertainty.

Additionally, we will try to introduce uncertainty-quantification deep learning methods to enhance the accuracy and reliability of 3D MPM.

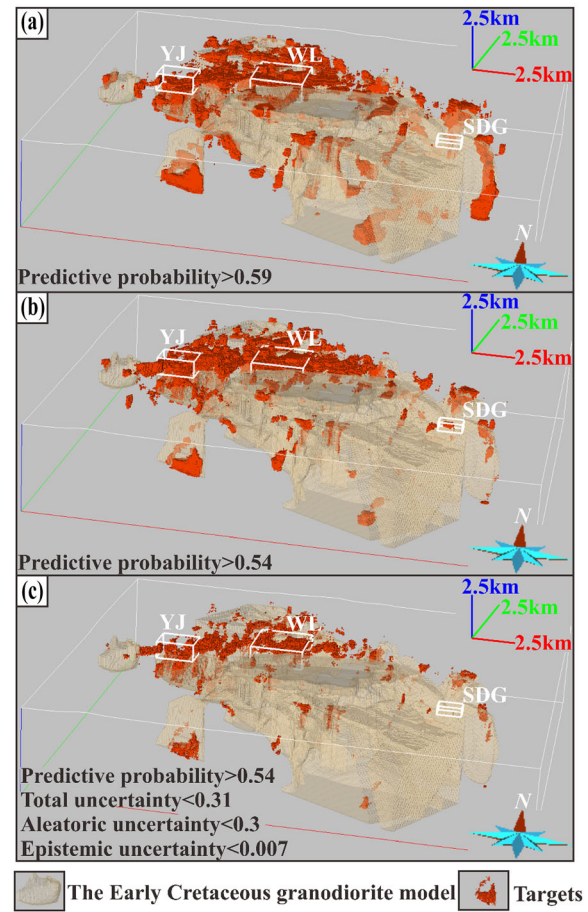


**Figure 14.** 3D exploration targets of the **a** RF model and **b** UQRF model delineated via the P–A plot; **c** 3D exploration targets of the UQRF model delineated via the P–A plot and accuracy–rejection curve.

## ACKNOWLEDGMENTS

This research is supported by Hebei Natural Science Foundation (No. D2023403051), Open Project Program of Hebei Province Collaborative Innovation Center for Strategic Critical Mineral Research, Hebei GEO University, China (No. HGEXT-2023-13), and the MNR Key Laboratory



# An Uncertainty-Quantification Machine Learning Framework for Data-Driven

for Exploration Theory & Technology of Critical Mineral Resources (No. 202405).

## DECLARATIONS

**COMPETING INTERESTS** Authors disclose non-financial interests are directly or indirectly related to this work submitted for publication.

## REFERENCES

- Agterberg, F. P. (1989). Computer programs for mineral exploration. *Science*, 245, 7681.
- Anderson, E. D., Monecke, T., Hitzman, M. W., Zhou, W., & Bedrossian, P. A. (2017). Mineral potential mapping in an accreted island-arc setting using aeromagnetic data: An example from Southwest Alaska. *Economic Geology*, 112, 375–396.
- Bergstra, J., Yamins, D. & Cox, D. D. (2013). Hyperopt: a python library for optimizing the hyperparameters of machine learning algorithms. In *Proceedings of the 12th Python in science conference*, 13, 20. Citeseer.
- Breiman, L. (2001). Random forests. *Machine Learning*, 45, 5s32.
- Burkin, J. N., Lindsay, M. D., Occhipinti, S. A., & Holden, E. J. (2019). Incorporating conceptual and interpretation uncertainty to mineral prospectivity modelling. *Geoscience Frontiers*, 10(4), 1383–1396.
- Carranza, E. J. M. (2008). *Geochemical Anomaly and Mineral Prospectivity Mapping in GIS* (p. 11). New York: Elsevier.
- Carranza, E. J. M., & Hale, M. (2001). Geologically constrained fuzzy mapping of gold mineralization potential, Baguio district, Philippines. *Natural Resources Research*, 10, 125–136.
- Carranza, E. J. M., & Laborte, A. G. (2015). Data-driven predictive mapping of gold prospectivity, Baguio district, Philippines: Application of Random Forests algorithm. *Ore Geology Reviews*, 71, 777–787.
- Deng, H., Zheng, Y., Chen, J., Yu, S., Xiao, K., & Mao, X. (2022). Learning 3D mineral prospectivity from 3D geological models using convolutional neural networks: Application to a structure-controlled hydrothermal gold deposit. *Computers & Geosciences*, 161, 105074.
- Du, B., Wang, Z., Santosh, M., Shen, Y., Liu, S., Liu, J., Xu, K., & Deng, J. (2023). Role of metasomatized mantle lithosphere in the formation of giant lode gold deposits: Insights from sulfur isotope and geochemistry of sulfides. *Geoscience Frontiers*, 14(5), 101587.
- Feng, H., Shen, P., Zhu, R., Tomkins, A. G., Brugger, J., Ma, G., Li, C., & Wu, Y. (2023). Bi/Te control on gold mineralizing processes in the North China Craton: Insights from the Wulong gold deposit. *Mineralium Deposita*, 58(2), 263–286.
- Gao, M., Wang, G., Carranza, E. J. M., Qi, S., Zhang, W., Pang, Z., Li, X., & Xiao, F. (2024). 3D Au targeting using machine learning with different sample combination and return-risk analysis in the Sanshandao-Cangshang District, Shandong Province, China. *Natural Resources Research*, 33, 51–74.
- Ghorbani, Y., Nwaila, G. T., Zhang, S. E., Bourdeau, J. E., Cánovas, M., Arzua, J., & Nikadat, N. (2023). Moving towards deep underground mineral resources: Drivers, challenges and potential solutions. *Resources Policy*, 80, 103222.
- Harris, J. R., Grunsky, E. C., Behnia, P., & Corrigan, D. (2015). Data-and knowledge-driven mineral prospectivity maps for Canada's North. *Ore Geology Reviews*, 71, 788–803.
- Huang, D., Zuo, R., & Wang, J. (2022). Geochemical anomaly identification and uncertainty quantification using a Bayesian convolutional neural network model. *Applied Geochemistry*, 146, 105450.
- Hüllermeier, E., & Waegeman, W. (2021). Aleatoric and epistemic uncertainty in machine learning: An introduction to concepts and methods. *Machine Learning*, 110, 457–506.
- Jordão, H., Sousa, A. J., & Soares, A. (2023). Using Bayesian neural networks for uncertainty assessment of ore type boundaries in complex geological models. *Natural Resources Research*, 32, 2495–2514.
- Kendall, A., & Gal, Y. (2017). What uncertainties do we need in Bayesian deep learning for computer vision? In *Advances in neural information processing systems* (Vol. 30).
- Kreuzer, O. P., Etheridge, M. A., Guj, P., McMahon, M. E., & Holden, D. J. (2008). Linking mineral deposit models to quantitative risk analysis and decision-making in exploration. *Economic Geology*, 103, 829–850.
- Li, R., Wang, G., & Carranza, E. J. M. (2016). GeoCube: A 3D mineral resources quantitative prediction and assessment system. *Computers & Geosciences*, 89, 161–173.
- Li, X., Xue, C., Chen, Y., Yuan, F., Li, Y., Zheng, C., Zhang, M., Ge, C., Guo, D., Lan, X., Tang, M., & Lu, S. (2023). 3D Convolutional Neural Network-based 3D mineral prospectivity modeling for targeting concealed mineralization within Chating area, middle-lower Yangtze River metallogenic Belt, China. *Ore Geology Reviews*, 157, 105444.
- Li, Y., & Oldenburg, D. W. (1996). 3-D inversion of magnetic data. *Geophysics*, 61(2), 394–408.
- Li, Y., & Oldenburg, D. W. (1998). 3-D inversion of gravity data. *Geophysics*, 63(1), 109–119.
- Lindsay, M. D., Piechocka, A. M., Jessell, M. W., Scalzo, R., Giraud, J., Pirot, G., & Cripps, E. (2022). Assessing the impact of conceptual mineral systems uncertainty on prospectivity predictions. *Geoscience Frontiers*, 13(6), 101435.
- Lisitsin, V. A., Porwal, A., & McCuaig, T. C. (2014). Probabilistic fuzzy logic modeling: quantifying uncertainty of mineral prospectivity models using Monte Carlo simulations. *Mathematical Geosciences*, 46, 747–769.
- Liu, J., Zhang, L., Wang, S., Li, T., Yang, Y., Liu, F., Li, S., & Duan, C. (2019). Formation of the Wulong gold deposit, Liaodong gold Province, NE China: Constraints from zircon U–Pb age, sericite Ar–Ar age, and H–O–S–He isotopes. *Ore Geology Reviews*, 109, 130–143.
- Lü, Q., Qi, G., & Yan, J. (2013). 3D geologic model of Shizishan ore field constrained by gravity and magnetic interactive modeling: A case history. *Geophysics*, 78(1), B25–B35.
- Malehmir, A., Thunehed, H., & Tryggvason, A. (2009). The Paleoproterozoic Kristineberg mining area, northern Sweden: Results from integrated 3D geophysical and geologic modeling, and implications for targeting ore deposits. *Geophysics*, 74(1), B9–B22.
- Manzi, M., Cooper, G., Malehmir, A., Durrheim, R., & Nkosi, Z. (2015). Integrated interpretation of 3D seismic data to enhance the detection of the gold-bearing reef: Mponeng Gold mine, Witwatersrand Basin (South Africa). *Geophysical Prospecting*, 63(4-Hard Rock Seismic imaging), 881–902.
- Mao, X., Liu, P., Deng, H., Liu, Z., Li, L., Wang, Y., Ai, Q., & Liu, J. (2023a). A novel approach to three-dimensional inference and modeling of magma conduits with exploration data: A case study from the Jinchuan Ni–Cu sulfide deposit, NW China. *Natural Resources Research*, 32, 901–928.
- Mao, X., Wang, J., Deng, H., Liu, Z., Chen, J., Wang, C., & Liu, J. (2023b). Bayesian decomposition modelling: An interpretable nonlinear approach for mineral prospectivity mapping. *Mathematical Geosciences*, 55, 897–942.
- McCuaig, T. C., Beresford, S., & Hronsky, J. (2010). Translating the mineral systems approach into an effective exploration targeting system. *Ore Geology Reviews*, 38(3), 128–138.

- Nielsen, S. H. H., Partington, G. A., Franey, D., & Dwight, T. (2019). 3D mineral potential modelling of gold distribution at the Tampia gold deposit. *Ore Geology Reviews*, 109, 276–289.
- Payne, C. E., Cunningham, F., Peters, K. J., Nielsen, S., Puccioni, E., Wildman, C., & Partington, G. A. (2015). From 2D to 3D: Prospectivity modelling in the Taupo volcanic zone, New Zealand. *Ore Geology Reviews*, 71, 558–577.
- Porwal, A., Carranza, E. J. M., & Hale, M. (2006). A hybrid fuzzy weights-of-evidence model for mineral potential mapping. *Natural Resources Research*, 15, 1–14.
- Porwal, A., Gonzalez-Alvarez, I., Markwitz, V., McCuaig, T. C., & Mamuse, A. (2010). Weights-of-evidence and logistic regression modeling of magmatic nickel sulfide prospectivity in the Yilgarn Craton, Western Australia. *Ore Geology Reviews*, 38(3), 184–196.
- Senge, R., Bösner, S., Dembczyński, K., Haasenritter, J., Hirsch, O., Donner-Banzhoff, N., & Hüllermeier, E. (2014). Reliable classification: Learning classifiers that distinguish aleatoric and epistemic uncertainty. *Information Sciences*, 255, 16–29.
- Shaker, M. H., & Hüllermeier, E. (2020). Aleatoric and epistemic uncertainty with random forests. In *Advances in intelligent data analysis XVIII: 18th international symposium on intelligent data analysis, IDA 2020, Konstanz, Germany, April 27–29, 2020, proceedings 18* (pp. 444–456). Springer.
- Smith, L. N. (2018). A disciplined approach to neural network hyper-parameters: Part 1—learning rate, batch size, momentum, and weight decay. arXiv preprint [arXiv:1803.09820](https://arxiv.org/abs/1803.09820).
- Wang, G., Li, R., Carranza, E. J. M., Zhang, S., Yan, C., Zhu, Y., Qu, J., Hong, D., Song, Y., Han, J., Ma, Z., Zhang, H., & Yang, F. (2015). 3D geological modeling for prediction of subsurface Mo targets in the Luanchuan district, China. *Ore Geology Reviews*, 71, 592–610.
- Wang, J., & Zuo, R. (2023). A Monte Carlo-based workflow for geochemical anomaly identification under uncertainty and global sensitivity analysis of model parameters. *Mathematical Geosciences*, 55(8), 1075–1099.
- Wang, Z., Yin, Z., Caers, J., & Zuo, R. (2020). A Monte Carlo-based framework for risk-return analysis in mineral prospectivity mapping. *Geoscience Frontiers*, 11(6), 2297–2308.
- Wei, J., Liu, C., & Tang, H. (2003). Rb-Sr and U-Pb isotopic systematics of pyrite and granite in Liaodong gold province, North China: Implication for the age and genesis of a gold deposit. *Geochemical Journal*, 37(5), 567–577.
- Wu, F., Yang, J., Wilde, S. A., & Zhang, X. (2005). Geochronology, petrogenesis and tectonic implications of Jurassic granites in the Liaodong Peninsula. *NE China. Chemical geology*, 221(1–2), 127–156.
- Wyborn, L. A. I., Heinrich, C. A., & Jaques, A. L. (1994). Australian Proterozoic mineral systems: essential ingredients and mappable criteria. In *Australian Institute of Mining and Metallurgy annual conference, Melbourne, proceedings* (pp. 109–115).
- Xiang, J., Xiao, K., Carranza, E. J. M., Chen, J., & Li, S. (2020). 3D mineral prospectivity mapping with random forests: A case study of Tongling, Anhui, China. *Natural Resources Research*, 29, 395–414.
- Xiong, Y., & Zuo, R. (2018). GIS-based rare events logistic regression for mineral prospectivity mapping. *Computers & Geosciences*, 111, 18–25.
- Yang, F., Wang, Z., Zuo, R., Sun, S., & Zhou, B. (2023). Quantification of uncertainty associated with evidence layers in mineral prospectivity mapping using direct sampling and convolutional neural network. *Natural Resources Research*, 32, 79–98.
- Yong, B. X., & Brintrup, A. (2022). Bayesian autoencoders with uncertainty quantification: Towards trustworthy anomaly detection. *Expert Systems with Applications*, 209, 118196.
- Yousefi, M., & Carranza, E. J. M. (2015). Prediction-area (P-A) plot and C-A fractal analysis to classify and evaluate evidential maps for mineral prospectivity modeling. *Computers & Geosciences*, 79, 69–81.
- Yousefi, M., Lindsay, M. D., & Kreuzer, O. (2024). Mitigating uncertainties in mineral exploration targeting: Majority voting and confidence index approaches in the context of an exploration information system (EIS). *Ore Geology Reviews*, 165, 105930.
- Yu, B., Zeng, Q., Frimmel, H. E., Qiu, H., Li, Q., Yang, J., Wang, Y., Zhou, L., Chen, P., & Li, J. (2020). The 127 Ma gold mineralization in the Wulong deposit, Liaodong Peninsula, China: constraints from molybdenite Re-Os, monazite U-Th-Pb, and zircon U-Pb geochronology. *Ore Geology Reviews*, 121, 103542.
- Yu, B., Zeng, Q., Frimmel, H. E., Wang, Y., Guo, W., Sun, G., Zhou, T., & Li, J. (2018). Genesis of the Wulong gold deposit, northeastern North China Craton: Constraints from fluid inclusions, HOS-Pb isotopes, and pyrite trace element concentrations. *Ore Geology Reviews*, 102, 313–337.
- Yuan, F., Li, X., Zhang, M., Jowitt, S. M., Jia, C., Zheng, T., & Zhou, T. (2014). Three-dimensional weights of evidence-based prospectivity modeling: A case study of the Baixiangshan mining area, Ningwu Basin, Middle and Lower Yangtze Metallogenic Belt, China. *Journal of Geochemical Exploration*, 145, 82–97.
- Zhang, H., Quost, B., & Masson, M. H. (2023a). Cautious weighted random forests. *Expert Systems with Applications*, 213, 118883.
- Zhang, P., Kou, L., Zhao, Y., Bi, Z., Sha, D., Han, R., & Li, Z. (2020a). Genesis of the Wulong gold deposit, Liaoning Province, NE China: Constrains from noble gases, radiogenic and stable isotope studies. *Geoscience Frontiers*, 11(2), 547–563.
- Zhang, S., Zhu, G., Xiao, S., Su, N., Liu, C., Wu, X., Yin, H., & Lu, Y. (2020b). Temporal variations in the dynamic evolution of an overriding plate: Evidence from the Wulong area in the eastern North China Craton. *China. GSA Bulletin*, 132(9–10), 2023–2042.
- Zhang, W., Wu, C., Zhong, H., Li, Y., & Wang, L. (2021a). Prediction of undrained shear strength using extreme gradient boosting and random forest based on Bayesian optimization. *Geoscience Frontiers*, 12(1), 469–477.
- Zhang, Z., Wang, G., Carranza, E. J. M., Fan, J., Liu, X., Zhang, X., Dong, Y., Chang, X., & Sha, D. (2022). An integrated framework for data-driven mineral prospectivity mapping using bagging-based positive-unlabeled learning and Bayesian cost-sensitive logistic regression. *Natural Resources Research*, 31, 3041–3060.
- Zhang, Z., Wang, G., Carranza, E. J. M., Liu, C., Li, J., Fu, C., Fan, J., & Dong, Y. (2023b). An integrated machine learning framework with uncertainty quantification for three-dimensional lithological modeling from multi-source geophysical data and drilling data. *Engineering Geology*, 324, 107255.
- Zhang, Z., Wang, G., Carranza, E. J. M., Zhang, J., Tao, G., Zeng, Q., Sha, D., Li, D., Shen, J., & Pang, Z. (2019). Metallogenic model of the Wulong gold district, China, and associated assessment of exploration criteria based on multi-scale geo-science datasets. *Ore Geology Reviews*, 114, 103138.
- Zhang, Z., Wang, G., Liu, C., Cheng, L., & Sha, D. (2021b). Bagging-based positive-unlabeled learning algorithm with Bayesian hyperparameter optimization for three-dimensional mineral potential mapping. *Computers & Geosciences*, 154, 104817.

## An Uncertainty-Quantification Machine Learning Framework for Data-Driven

- Zheng, F., Xu, T., Ai, Y., Yang, Y., Zeng, Q., Yu, B., Zhang, W., & Xie, T. (2022). Metallogenic potential of the Wulong goldfield, Liaodong Peninsula, China revealed by high-resolution ambient noise tomography. *Ore Geology Reviews*, 142, 104704.
- Zhou, X., Wen, H., Zhang, Y., Xu, J., & Zhang, W. (2021). Landslide susceptibility mapping using hybrid random forest with GeoDetector and RFE for factor optimization. *Geoscience Frontiers*, 12(5), 101211.
- Zuo, R., Kreuzer, O. P., Wang, J., Xiong, Y., Zhang, Z., & Wang, Z. (2021). Uncertainties in GIS-based mineral prospectivity mapping: Key types, potential impacts and possible solutions. *Natural Resources Research*, 30, 3059–3079.
- Zuo, R., Xiong, Y., Wang, Z., Wang, J., & Kreuzer, O. P. (2023). A new generation of artificial intelligence algorithms for mineral prospectivity Mapping. *Natural Resources Research*. <https://doi.org/10.1007/s11053-023-10237-w>.
- Zuo, R., Zhang, Z., Zhang, D., Carranza, E. J. M., & Wang, H. (2015). Evaluation of uncertainty in mineral prospectivity mapping due to missing evidence: a case study with skarn-type Fe deposits in Southwestern Fujian Province, China. *Ore Geology Reviews*, 71, 502–515.
- Springer Nature or its licensor (e.g. a society or other partner) holds exclusive rights to this article under a publishing agreement with the author(s) or other rightsholder(s); author self-archiving of the accepted manuscript version of this article is solely governed by the terms of such publishing agreement and applicable law.